

# Compressive MRI quantification using convex spatiotemporal priors and deep auto-encoders

Mohammad Golbabaee, *Member, IEEE*, Guido Bounincontri, Carolin M. Pirkel,  
Marion I. Menzel, Bjoern H. Menze, Mike Davies and Pedro A. Gómez

**Abstract**—We propose a dictionary-matching-free pipeline for multi-parametric quantitative MRI image computing. Our approach has two stages based on compressed sensing reconstruction and deep learned quantitative inference. The reconstruction phase is convex and incorporates efficient spatiotemporal regularisations within an accelerated iterative shrinkage algorithm. This minimises the under-sampling (aliasing) artefacts from aggressively short scan times. The learned quantitative inference phase is purely trained on physical simulations (Bloch equations) that are flexible for producing rich training samples. We propose a deep and compact auto-encoder network with residual blocks in order to embed Bloch manifold projections through multi-scale piecewise affine approximations, and to replace the non-scalable dictionary-matching baseline. Tested on a number of datasets we demonstrate effectiveness of the proposed scheme for recovering accurate and consistent quantitative information from novel and aggressively subsampled 2D/3D quantitative MRI acquisition protocols.

**Index Terms**—MR Fingerprinting, compressed sensing, convex model-based reconstruction, residual network, auto-encoder.

## I. INTRODUCTION

Quantification of the intrinsic NMR characteristics [1] has proven powerful for tissue identification and tracking pathological changes. Despite many potentials, standard quantitative MRI (QMRI) approaches have very long acquisition times and for this reason, are not widely applicable in clinical setups. Magnetic Resonance Fingerprinting (MRF) has emerged to overcome this challenge [2]. MRF uses short excitation sequences capable of simultaneously encoding multitudes of NMR properties and further adopts Compressed Sensing (CS) to subsample a tiny fraction of the spatiotemporal k-space information [3, 4, 5, 6, 7]. Estimating the underlying quantitative maps therefore becomes a highly ill-posed inverse problem.

Popular computational approaches to the MRF inverse problem rely on *dictionary matching* (DM), primarily for parameter inference i.e. estimating quantitative maps from back-projected images, or further for promoting temporal-domain priors within model-based MRF reconstructions to reduce undersampling artefacts [8, 9]. However DM's complexity (storage/runtime) does not scale well to the emerging multi-parametric QMRI applications. *Deep learning* MRF approaches recently emerged to address this issue [10, 11, 12]. Back-projected images are fed into a compact neural network that temporally processes voxel-wise MRF signal evolutions,

so-called fingerprints, and replaces DM for quantitative inference. Trained with independently corrupted noisy fingerprints, such networks are unable to correct for dominant spatially-correlated (aliasing) artefacts appearing in heavily undersampled acquisitions. While larger convolutional models [13, 14, 15] capture spatiotemporal information to resolve aliasing artefacts, labelled QMRI datasets (i.e. ground-truth multi-parametric maps) that are necessary to train these models particularly in novel applications are scarce and hence place adaption of these models at the risk of overfitted predictions. Further, current approaches along this line build customised de-noisers (de-aliasing) and require expensive re-training by changing sampling parameters i.e. the forward model.

This work aims to address these shortcomings through a two-stage DM-free pipeline: First, we take a CS approach to *spatiotemporally process* the k-space data and minimise undersampling artefacts in the reconstructed image time-series, and second we feed the resulted sequence to a deep and compact *auto-encoder* network with *residual blocks* for per-voxel quantitative inference. We cast reconstruction as a *convex* optimisation problem (LRTV) which enjoys reproducible global solutions regardless of initialisation and can be implemented with a momentum-accelerated algorithm with fast convergence. Spatial regularities of the MRF time-series are promoted by the *Total Variation* shrinkage and temporal structures are relaxed to an a-priori learned *low-rank factorised* model. We further provide geometrical insights to the mechanism behind the proposed deep inference approach. We show that the network provides a *multi-resolution piecewise affine approximation* to the Bloch response manifold projection. Rather than memorising a large MRF dictionary, the network hierarchically clusters this manifold through deep layers and learns a compact set of *deep regressing filters* for parameter inference. The proposed pipeline is validated on a number of experiments using a novel multi-parametric acquisition sequence for *2D and 3D quantitative brain imaging*. Our approach can flexibly apply and report consistent predictions for different k-space readouts and further outperforms shallow learned inference models related to the Gaussian kernel fitting.

**Paper organisation:** We review previous related works in section II. Section III presents the inverse imaging problem model. Section IV presents our reconstruction and quantitative inference pipeline. Section V presents our geometrical insight to the network's performance for deep quantitative inference. In Section VI we present and discuss our experimental results, and finally we conclude in section VII.

MG is with the Computer Science department at the University of Bath, UK: (m.golbabaee@bath.ac.uk). GB is with Imago7 foundation. MD is with the University of Edinburgh. MIM is with the GE Healthcare. CMP, BHM and PAG are with the Technical University of Munich.

*Notations:* Throughout  $\|\cdot\|$  denotes the Euclidean norm of a vector or a matrix,  $\|\cdot\|_{TV}$  denotes the Total Variation (TV) of a 2D or 3D spatial image defined by the sums of its gradient magnitudes [16]. Matrix rows and columns are denoted by  $X_{(i,\cdot)}$  and  $X_i$  respectively.

## II. RELATED WORKS

Here we highlight a number of related computational approaches for the MRF problem. Multi-parametric quantification based on fingerprinting, DM and its SVD-compressed (low-rank) variant were proposed in [2, 17]. Reconstructing image time-series from k-space data was non-iterative and used zero-filling (ZF). Inspired by CS, later studies adopted model-based reconstructions to reduce subsampling (aliasing) artefacts and to pave the path for aggressively shorter scan times [8, 9]. These methods are based on non-convex optimisation (iterative) without momentum-acceleration, and require DM per iteration in order to promote temporal-domain priors according to the Bloch dynamics. To accelerate DM's runtime, fast search schemes based on grouping the fingerprints [18] or forming tree structures were proposed [19, 20]. Nonetheless the large size of the MRF dictionary remained a storage challenge to all. For some k-space subsampling patterns, including those adopted in our experiments, using only a temporal-domain prior is insufficient to produce artefact-free reconstructions (see e.g. [19, 20]). This issue was tackled by low-pass filtering [19] that traded off images sharpness and later was improved by a Total Variation (TV) regularisation [21]. Nonetheless both methods require DM per-iteration, are nonconvex and without momentum-acceleration. DM-free convex reconstructions based on low-rank priors were proposed in [22, 23] (albeit cascaded to DM for quantitative inference), however [22] does not incorporate spatial domain priors and [23] encounters the cost of per-iteration SVD decompositions. We avoid this and add spatial TV regularisation for dimension-reduced image time-series while enforcing temporal-domain priors through a (low-rank) subspace representation of the dictionary instead of DM.

On the other hand, deep learning MRF approaches recently emerged to address the non-scalability of DM. Many works use the ZF reconstruction baseline and for quantitative inference they replace DM with a neural network. These methods broadly divide in two camps: the first group learns temporal-domain dynamics from simulating Bloch equations; hence is rich with training data (see e.g. [10, 11, 12, 24] and also a kernel machine approach for shallow learning [25]). The second group use convolutional layers to also learn spatial domain regularities, see e.g. [13, 14, 15], but they require training on ground truth quantitative anatomical maps that may not be largely available as for the mainstream qualitative MRI. Our quantitative inference approach belongs to the first camp; we however replace ZF by a DM-free spatiotemporally regularised (model-based) reconstruction to remove undersampling artefacts before being fed to the network.

## III. COMPRESSIVE QMRI ACQUISITION MODEL

The compressed sensing approach adopted by MRF for acquiring quantitative information follows a linear spatiotem-

poral model [2]:

$$Y = \mathcal{A}(\bar{X}) + \xi, \quad (1)$$

where  $Y \in \mathbb{C}^{T \times m}$  is the multi-coil k-space measurements collected at  $t = 1, \dots, T$  temporal frames and corrupted by some noise  $\xi$ . The Time-Series of Magnetisation Images (TSMI)—to be reconstructed—is an image sequence represented by a complex-valued matrix  $\bar{X}$  of spatiotemporal resolution  $T \times n$  i.e.  $n$  spatial voxels across  $T$  temporal frames. The forward operator  $\mathcal{A} := F_\Omega S$  models the multi-coil sensitivities operator  $S$ , and the Fourier transform  $F$  subsampled according to a set of *temporally-varying* k-space locations  $\Omega$ .

The tissues' quantitative properties in each voxel are encoded in a temporal signal at the corresponding column of the TSMI matrix. This signal records the magnetisation response of proton dipoles to dynamic *excitations* in the form a sequence of flip angles (magnetic field rotations) applying with certain repetition (TR) and echo (TE) times. Tissues with different NMR characteristics respond distinctively to excitations. QMRI/MRF rely on this principle to estimate quantitative characteristics from the (computed) TSMI. Per-voxel  $v$  magnetisation responses of the TSMI scaled by the *proton density*  $\gamma_v$  are modelled as

$$X_v \approx \gamma_v \mathcal{B}(\Theta_v) \quad \forall v \in 1, \dots, n \quad (2)$$

where the *Bloch response*  $\mathcal{B}(\Theta_v) : \mathbb{R}^p \rightarrow \mathbb{C}^T$  is a non-linear mapping from per-voxel intrinsic NMR properties  $\Theta_v$  to the corresponding (discrete-time) solution of the *Bloch differential equations* which captures the overall transient-state macroscopic dynamics of a voxel [26]. Our experiments use sequences that simultaneously encode  $p = 2$  characteristics in each voxel i.e. the T1 and T2 relaxation times. This could be further extended to include other properties e.g. off resonance frequencies,  $T2^*$ , diffusion and perfusion [4, 5, 6].

### A. Low-dimensional manifold and subspace models

Estimating  $\Theta$  (i.e. quantification) requires long enough sequences  $T > p$  to create contrast between different tissues' responses. As such the Bloch responses despite their high ambient dimension live on a *low  $p$ -dimensional (nonlinear) sub-manifold* of  $\mathbb{C}^T$ . Further it is observed that for certain excitation sequences, including those used in our experiments, this manifold is approximately embedded in a *low-rank subspace*  $\text{Range}(V) \subset \mathbb{C}^T$  represented by an orthonormal matrix  $V \in \mathbb{C}^{T \times s}$  where  $p < s \ll T$ . Hence the following dimension-reduced alternatives for models (1) and (2) can be deduced:

$$Y \approx \mathcal{A}(VX) \quad (3)$$

$$X_v \approx \gamma_v V^H \mathcal{B}(\Theta_v) \quad (4)$$

where  $X \in \mathbb{C}^{s \times n}$  is the dimension-reduced TSMI. This compact representation is the basis for the subspace compression methods [9, 22] and is proven beneficial to the runtime and accuracy (by noise trimming) of the reconstructions.

### B. Model-fitting for parameter inference

Fitting computed TSMIs to the Bloch response model is central to QMRI. Per-voxel model-fitting according to (4) for

obtaining the NMR characteristics and proton density reads (see e.g. [17, 8]):

$$\hat{\Theta}_v = \mathcal{P}_B(\hat{X}_v) := \operatorname{argmin}_{\Theta} \|\hat{X}_v - V^H \mathcal{B}(\Theta)\| \quad (5)$$

$$\hat{\gamma}_v = \langle \hat{X}_v, V^H \mathcal{B}(\hat{\Theta}_v) \rangle \quad (6)$$

We assumed without losing generality having normalised Bloch responses. We refer to  $\mathcal{P}_B(\cdot)$  as the *Bloch response manifold projection*. This projection is nonconvex and oftentimes intractable for the generally complicated Bloch responses adopted by the MRF sequences. The MRF framework instead approximates (5) by *dictionary matching* (DM). A *fingerprint dictionary*  $D = \{D_j\}$  is constructed for sampling the manifold of Bloch responses through a fine-grid discretisation of the parameter space  $[\Theta] = [T1] \times [T2] \times \dots$  and exhaustively simulating the Bloch responses  $D_j := \mathcal{B}([\Theta_j])$  for all combinations of the quantised parameters. The DM step identifies the most correlated fingerprint (and the underlying NMR parameters) for each voxel of the reconstructed TSMI:

$$\mathcal{P}_B(\hat{X}_v) \approx \operatorname{argmin}_j \|\hat{X}_v - V^H D_j\| \quad (7)$$

through a nearest neighbour *search* that is itself a projection onto the discrete set of fingerprints i.e. a *point-wise approximation* to the (continuous) Bloch response manifold.

Viewing fingerprints as training samples, the dictionary can be factorised through principal component analysis (PCA) [17]:

$$DD^H \approx V \Lambda V^H \quad (8)$$

for unsupervisedly learning the low-rank subspace representation of the Bloch responses. This representation helps to reduce temporal dimension and can be coupled with fast search schemes [18, 20, 19] to accelerate DM runtime. However any form of DM (fast or exhaustive search) remains non-scalable and creates storage overhead in multi-parametric QMRI applications because the number of dictionary atoms *exponentially* grows with  $p$ .

#### IV. DM-FREE IMAGE RECONSTRUCTION AND PARAMETER INFERENCE PIPELINE

Our DM-free image computing pipeline consists of two stages: i) reconstructing TSMIs from undersampled k-space measurements and then ii) approximate model-fitting according to (4) for parameter inference. A set of simulated fingerprints (could be MRF dictionary) sample the Bloch response model and are used only for training (pre-processing) in order to learn three temporal-domain models: i) a dimension-reduced (low-rank) subspace representation for the Bloch responses, ii) an encoder network to map noisy fingerprints to the NMR parameters, and iii) a decoder network to generate clean Bloch responses from the NMR parameters.

##### A. Convex TSMI reconstruction with LRTV algorithm

A popular MRF baseline uses zero-filling (ZF) [17], that is back-projecting k-space measurements to form a dimension-reduced TSMI through the adjoint of (3):

$$\hat{X} = V^H \mathcal{A}^H(Y) \in \mathbb{C}^{s \times n} \quad (9)$$

prior to the DM inference. Modern QMRI/MRF acquisitions aggressively curtail the scan times by using short excitation sequences and severe spatial (k-space) subsampling. As such the inverse problem (1) becomes highly ill-posed and ZF (which is not an inversion) results in aliasing artefacts in the reconstructed TSMI. Errors made at this stage can be indeed significant (see experiment results), they propagate to the parameter inference step and deteriorate the overall quantification accuracy.

To address this issue, we adopt model-based CS reconstruction with simultaneous spatiotemporal regularisations. Dimension-reduced TSMIs are computed through solving the following convex and DM-free optimisation dubbed as LRTV:

$$\hat{X} = \operatorname{argmin}_{X \in \mathbb{C}^{s \times n}} \|Y - \mathcal{A}(VX)\|^2 + \sum_{i=1}^s \lambda_i \|X_{(i, \cdot)}\|_{TV} \quad (10)$$

The first term minimises discrepancies between the k-space measurements and the solutions through the factorised forward model (3). As such LRTV adopts a temporal-domain prior through the subspace model (i.e. the low-rank factorisation  $\bar{X} \approx VX$ ) which provides a compact and convex (in fact linear) *relaxed representation* for the Bloch response model instead of using the MRF dictionary. LRTV additionally adopts Total Variation (TV) regularisation. Each component of the TSMI corresponds to a spatial 2D or 3D volumetric image  $X_{(i, \cdot)}$  (matrix row), where penalising its TV norm promotes spatial-domain regularities via sparse image gradients [16].  $\lambda_i > 0$  control per (subspace) component regularisation levels.

The LRTV problem (10) can be efficiently solved using Fast Iterative Shrinkage Algorithm with Nesterov-type momentum acceleration and backtracking step-size [27, 28]. Each iteration  $k = 0, 1, 2 \dots$  computes:

$$\begin{cases} \nabla = X^k - \mu_k V^H \mathcal{A}^H (\mathcal{A}(VX^k) - Y) \\ Z_{(i, \cdot)}^k = \mathbf{Prox}_{\lambda_i \mu_k}(\nabla_{(i, \cdot)}) \quad \forall i = 1, \dots, s \\ X^{k+1} = Z^k + \left(\frac{k-1}{k+2}\right) (Z^k - X^{k-1}) \end{cases} \quad (11)$$

The first and third lines correspond to the gradient and momentum-acceleration updates, respectively. The second line computes a small number  $s \ll T$  of shrinkage operations for the 2D/3D images in each subspace component  $\mathbf{Prox}_{\alpha}(x) := \operatorname{argmin}_u \frac{1}{2} \|x - u\|^2 + \alpha \|u\|_{TV}$ , which can be efficiently done on a GPU using the Primal-Dual algorithm [29]. Per iteration, the initial step size  $\mu_k$  halves until the following criteria holds:<sup>1</sup>

$$\begin{aligned} \|Y - \mathcal{A}(VZ^k)\|^2 &> \|Y - \mathcal{A}(VX^k)\|^2 + \\ &2\operatorname{Re}\langle G, Z^k - X^k \rangle + \mu_k^{-1} \|Z^k - X^k\|^2 \end{aligned}$$

With an all-zero initialisation, the first line of (11) recovers ZF in the first iteration. Setting  $\lambda = 0$  recovers the LR problem [22] that is a convex relaxed alternative to the BLIP [8], wherein temporal-only priors based on the MRF dictionary are replaced by the low-rank subspace. Note that the size of  $V$  is independent of the number of fingerprints (used for training). Hence the solver does not face a memory bottleneck and the slow progress of computing DM per iteration. While for certain (Cartesian) sampling schemes this temporal model

<sup>1</sup>Optional warm-start could rescale the chosen  $\mu_1$  by factor  $\|Y\|/\|\mathcal{A}(X^1)\|$ .

can decently regularise the inversion [30], for other important sampling patterns e.g. non-cartesian spiral and radial readouts used in our experiments, it turns out to be inadequate and fails to output artefact-free TSMIs (see section VI). Multi-prior CS solvers are proven effective for highly undersampled systems by further restricting degrees of freedom of data [31, 32]. The LRTV uses this fact by setting  $\lambda > 0$  and adding spatial priors to sufficiently regularise the problem. Besides being DM-free, the proposed approach has other advantages over its non-convex alternatives including a tractable way to incorporate multiple priors<sup>2</sup>, momentum-acceleration for fast convergence and reproducible global solutions regardless of initialisation.

### B. MRFResnet for parameter inference

Instead of using a large-size dictionary for DM, we propose training and using a compact network coined as *MRFResnet* in the form of an auto-encoder with deep residual blocks, shown in Figure 1. Auto-encoders have proven powerful in denoising tasks through creating an *information bottleneck* which corresponds to learning a low-dimensional manifold model for capturing (nonlinear) intrinsic signal structures [33]. In our task computed TSMI voxels are processed by such a model to create clean magnetisation responses as well as estimating the intrinsic NMR parameters in a computably efficient manner. The  $p = 2$  neurons bottleneck (in Figure 1) has a physical interpretation: fitting noisy temporal trajectories to the nonlinear Bloch model with limited  $p \ll T$  degrees of freedom determined by the T1 and T2 quantities.

1) *Encoder*: This network learns to approximate Bloch manifold projections through a continuous mapping  $\mathcal{R} : \hat{X}_v \rightarrow \Theta_v$  parametrised by the network's weights and biases  $\{W, \beta\}$ :

$$\mathcal{R}(x) \equiv h^{(N+1)}(x) = \varphi \left( W^{(N+1)} h^{(N)}(x) + \beta^{(N+1)} \right) \quad (12)$$

where  $h^{(i)}$  the outputs of  $i = 1, \dots, N$  residual blocks are

$$\begin{aligned} h^{(i)}(x) &= \varphi \left( h^{(i-1)}(x) + g^{(i)}(x) \right), \\ g^{(i)}(x) &= W^{(i,2)} \varphi \left( W^{(i,1)} h^{(i-1)}(x) + \beta^{(i,1)} \right) + \beta^{(i,2)}, \end{aligned}$$

$h^{(0)}(x) = x$  and the ReLU activations  $\varphi(x) = \max(x, 0)$  are used throughout. The inputs are the normalised temporal voxels of the dimension-reduced TSMI. The network is trained on simulated noisy Bloch responses (see section VI-B) so that the approximate projection holds

$$\mathcal{R}(x) \approx \mathcal{P}_{\mathcal{B}}(x) \quad (13)$$

in a neighbourhood of the (compressed) Bloch manifold.

2) *Decoder*: The proton density (PD) is a scaling factor that amplifies the Bloch responses in each voxel. Hence after estimating other nonlinear NMR parameters (e.g. T1/T2) using the encoder part, PD can be explicitly resolved through (6). This would however require evaluating/solving Bloch responses for

<sup>2</sup>In non-convex (e.g. DM-based) approaches incorporating extra priors such as spatial regularity constraints is not always algorithmically tractable e.g. sequential projections on two sets where one is non-convex may not result in projecting onto the intersection.

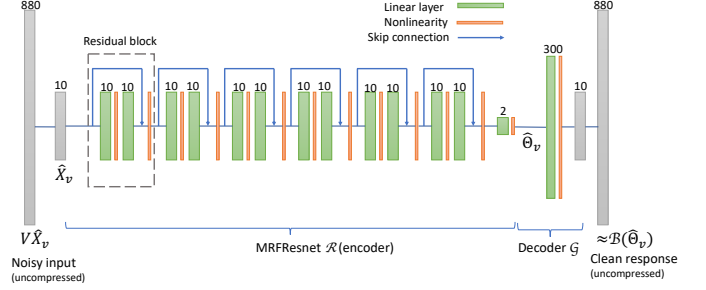


Fig. 1: MRFResnet (encoder) for T1/T2 inference, the Bloch response generative network  $\mathcal{G}$  (decoder), and the *implicit* linear dimensionality reduction/expansion (first/last) layers using the subspace model  $V^H/V$ .

all voxels and their parameters  $\Theta_v$  which can be computationally intensive. Instead we train a *decoder* network  $\mathcal{G}(\cdot)$  which for given NMR parameters it approximately generates

$$\mathcal{G}(\Theta_v) \approx V^H \mathcal{B}(\Theta_v) \quad (14)$$

the corresponding compressed Bloch responses (clean fingerprints) in short runtimes. This allows (6) to be easily applied without significant computations. For the sequence design used in our experiments, it turns out that a fully-connected shallow network with one hidden layer and ReLU activations can approximate well this step.<sup>3</sup> Unit dimensions are customised to a sequence used in our experiments encoding T1/T2 relaxation times, with reduced subspace dimension  $s = 10$ . Encoder has  $N = 6$  residual blocks of 10 neurons width, and decoder has 300 neurons in its single hidden layer.

The subspace compression helps reduce model sizes in both networks (hence reducing risk of overfitted predictions) and also reduce required training resources compared to uncompressed deep MRF approaches [10, 11]. Further to avoid losing discrimination between fingerprints —e.g. by a magnitude-only data processing [10]—we adopt a practical phase-alignment heuristic from [20, 19] to de-phase TSMIs and training samples before being fed to MRFResnet. This treatment allows the network without losing generality have real-valued parameters and approximate real-valued mappings.<sup>4</sup>

### V. HIERARCHICAL PARTITIONING OF THE BLOCH RESPONSE MANIFOLD

In this part we show that the MRFResnet provides a multi-scale piecewise affine approximation to the Bloch response manifold projection (5). Hierarchical partitioning and multi-scale approximations are also central to the fast search schemes proposed for the DM-based MRF (see illustrations in [20, 35]). However unlike any form of DM (fast or exhaustive) that creates point-wise approximations for (7), MRFResnet does not memorise a dictionary and rather uses it to learn and efficiently encode a compact set of partitions and *deep matched-filters* for affine regression of the NMR quantities.

<sup>3</sup>We also observed a similar network complexity for generating responses to the well-known FISP sequence [3]. However, we did not achieved accurate predictions using shallow architectures of comparable sizes for  $\mathcal{R}$  (two layer were needed at least however with larger model than MRFResnet [12, 34]). This suggests that generating clean responses (decoding) was easier than projecting noisy fingerprints to their generative parameters (encoding), and the latter requires deep processing (see section V).

<sup>4</sup>Another way is to duplicate input size by separating real and imaginary signal components e.g. [11]. We found this unnecessary in our experiments.



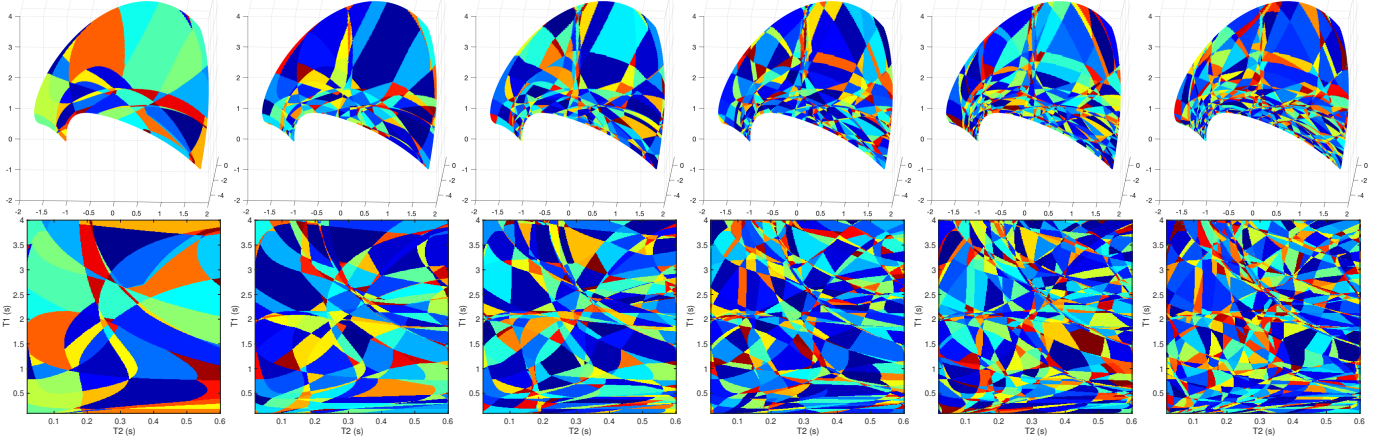


Fig. 2: Coarse-to-fine partitioning of the Bloch manifold (top row) sampled by a dense fingerprinting dictionary, and their generative T1/T2 parameters (bottom row), using MRFResnet. From left to right figures illustrate learned partitions after each residual block.

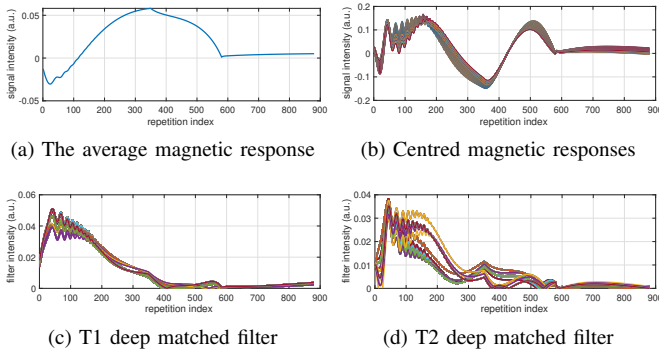


Fig. 3: (a) The mean and (b) centred Bloch responses within the range  $(T1, T2) \in [1000 - 1200] \times [80 - 110]$  (ms). (c)-(d) The end-to-end match filters learned by the MRFResnet to regress T1/T2 values are shown across the original (non-compressed) temporal dimension.

#### A. Affine spline function approximation

The MRFResnet encoder (also its decoder network) is composed of linear connections and piecewise linear ReLU activations. This results in piecewise affine functions  $h^{(i)}(x)$  after each residual block as well as the end-to-end mapping  $\mathcal{R}(x)$  (see e.g. [36, 37]). Further,  $\mathcal{R}$  is *Lipschitz continuous* for continuous activation functions as above and for bounded  $\{W^{(i)}, \beta^{(i)}, i\}$ .

**Theorem 1.** Denote by  $z : \mathbb{R}^s \rightarrow \mathbb{R}^p$

$$z(x) := W^{(N+1)}h^{(N)}(x) + \beta^{(N+1)} \quad (15)$$

the weighted outputs in (12) before the last non-linearity.<sup>5</sup> The following affine spline representation holds for MRFResnet:

$$z(x) = \mathbf{A}[x]x + \mathbf{b}[x] := \sum_r (A_r x + b_r) \iota_{\Omega_r}(x), \quad (16)$$

where  $\iota_{\Omega_r}(x)$  is the indicator function with respect to a segment (set)  $\Omega_r \in \mathbb{R}^s$ , returning  $x$  if it belongs to the segment and 0 otherwise —segments form a disjoint partitioning of the input space with affine boundaries. Matrices  $A_r \in \mathbb{R}^{p \times s}$  and vectors  $b_r \in \mathbb{R}^p$  define the corresponding slopes and offsets for the input-output affine mapping in each segment. Shorthands

<sup>5</sup>The last ReLU layer in  $\mathcal{R}$  is for imposing the positivity of T1/T2 values, and therefore the prediction task is mainly done by the preceding layers.

$\mathbf{A}[x] : \mathbb{R}^s \rightarrow \mathbb{R}^p$  and  $\mathbf{b}[x] : \mathbb{R}^s \rightarrow \mathbb{R}^p$  represent the input-dependent (piece-wise affine) mapping of  $z(x)$ .  $\mathbf{b}[x]$  represents  $p$  input-dependent offsets. Similarly,  $\mathbf{A}[x]$  is an input-dependent  $p \times s$  matrix where each row is a deep matched-filter returning its correlation with  $x$  for each output.

Proof can be found in [36] for general feedforward networks with fully-connected, convolutional, pooling and/or residual layers and using any piecewise-linear activations. During training, MRFResnet encoder learns  $\{W^{(i)}, \beta^{(i)}\}$  or equivalently  $\{\mathbf{A}[x], \mathbf{b}[x]\}$  to provide a continuous and piece-wise affine *approximation* for (5). The universal approximation theorem [38] states that a shallow network with one but very wide hidden layer can do this. Deeper networks are however more practical to efficiently reduce the number of hidden units [39]. Indeed, we experimentally observe this (section VI-C) by comparing MRFResnet to a shallow learning scheme related to [25] based on Kernel Machines (KM) and random features [40].

#### B. Visualising MRFResnet segments on Bloch manifold

**Remark 1.** Continuity of  $z(x)$  implies that adjacent segments  $\Omega_r, \Omega_{r'}$  correspond to distinct  $A_r, A_{r'}$ . Indeed, if  $A_r = A_{r'}$  and the only difference is in the offsets  $b_r \neq b_{r'}$ , then  $\Omega_r, \Omega_{r'}$  won't intersect on boundaries. Therefore they are not adjacent segments unless contradicting the continuity assumption.

This remark gives an idea for visualizing the input space segments. For densely sampled input signals  $x$ , we compute derivatives of the weighted outputs (15) with respect to inputs using *back propagation*. These will determine the input-dependent slopes in the affine spline formulation (16) i.e. rows of  $\mathbf{A}[x]$  at a point  $x$  are populated as follows  $\forall j = 1, 2, \dots, p$ :

$$\mathbf{A}[x]_{(j, \cdot)} = \left[ \frac{\partial z_j(x)}{\partial x_1}, \frac{\partial z_j(x)}{\partial x_2}, \dots, \frac{\partial z_j(x)}{\partial x_s} \right]. \quad (17)$$

By vector quantisation (e.g. k-means clustering) we cluster regions of  $x$  that output distinct slopes  $A_r$  and identify the segments  $\Omega_r$ . Similar routine could apply to compute input space partitions by clustering back-propagated output derivatives after each residual block (Theorem 1 and Remark 1 also hold for the intermediate blocks of  $\mathcal{R}$ ).

According to [36] as we progress into deeper layers, partitions will be subdivided into smaller segments in a *hierarchical*

fashion. This can be observed in Figure 2 where we adopted the above routine for the T1/T2 encoding MRF sequence used in our experiments and visualised multi-scale (from coarse-to-fine) partitions obtained after each residual layer. The Bloch response manifold is sampled across fine-gridded T1/T2 values (i.e. MRF dictionary) to visualise the intersection of the input space segments with this manifold (results are visualised across the three dominant principal component axes). MRFResnet encoder learns about a thousand partitions for its end-to-end mapping  $z(x)$ . In the light of (16) we know that for each partition  $\Omega_r$ , the network implicitly encodes  $p = 2$  deep matched-filters (the rows of  $\mathbf{A}[x]$  or alternatively  $A_r$ ) and an offset term to locally linearly regress the T1/T2 outputs in that segment. As such instead of memorising  $>100K$  dictionary atoms used for training, the network learns a compact piecewise affine approximation to the Bloch manifold projection (5) as a rapid and memory-efficient alternative to DM's point-wise approximation (7). The total number of parameters used by the MRFResnet (Table I) are two hundreds times less than the size of the dimension-reduced MRF dictionary. Figure 3 shows the Bloch responses for a range of T1/T2 values, as well as deep matched-filters learned by MRFResnet to predict each of these quantities in this range from noisy inputs. Computed through (17), match-filters are one-dimensional analogues of the *saliency maps* a.k.a. *deep dream images* [41], measuring sensitivities of the neurons with respect to the inputs.

## VI. NUMERICAL EXPERIMENTS AND DISCUSSIONS

### A. Datasets and 2D/3D acquisition parameters

Methods are tested on the Brainweb *in-silico* phantom (see supplementary materials), a EUROSPIN TO5 phantom (*in-vitro*) [42], and a healthy human brain (*in-vivo*). *In-vitro* and *in-vivo* data were acquired on a 1.5T GE HDxT scanner using 8-channel receive-only head RF coil. The novel adopted excitation sequence has  $T = 880$  repetitions and jointly encodes T1/T2 values using an inversion pulse followed by a flip angle schedule that linearly ramps up from  $1^\circ$  to  $70^\circ$  in repetitions 1-400, ramps down to  $1^\circ$  in repetitions 400-600, and then stays constant to  $1^\circ$  for repetitions 600-880 (see more details in [43]). Three non-Cartesian readout trajectories were tested: 2D/3D variable density spiral and 2D radial k-space subsampling patterns. Throughout we used  $T_{inv}=18$  ms, fixed  $TR=12$  ms, and  $TE = 0.46/2.08$  ms for spiral/radial acquisitions, respectively. For the 2D/3D acquisitions we had  $200^2/200^3$  ( $\text{mm}^2/\text{mm}^3$ ) FOV and  $200^2/200^3$  voxels image/tensor size, respectively. Further, the total number of interleaves for the 2D/3D spiral and 2D radial readouts were 377/48'400 and 967, respectively. The total acquisition times for the 2D and 3D scans were 10:56 seconds and 9:51 minutes, respectively.

### B. Tested algorithms

1) *TSMI reconstruction*: we compare model-based (convex) methods LRTV and LR through solving iteratively (10) with spatiotemporal ( $\lambda > 0$ ) and temporal-only ( $\lambda = 0$ ) regularisations, respectively. The latter is a convex relaxation of the BLIP algorithm [8]. Further we compare against non-iterative

baselines zero-filling (ZF) (9) and ViewSharing (VS) [44]. VS aggregates spatial k-space data within neighbouring temporal frames to increase per-frame samples and enhance spatial resolutions in a non model-based fashion. Coil sensitivities were computed from undersampled data using an adaptive coil combination scheme [45].

2) *Quantitative inference*: We compare learned models MRFResnet (deep learning) and a shallow learning method based on Gaussian Kernel Machines (KM) related to [25]. We further consider baselines DM and Fast Group Matching (FGM) [18] using exhaustive and fast dictionary searches, respectively.<sup>6</sup>

3) *Learned models*: All methods above use a  $s = 10$  dimensional subspace model a-priori learned from Bloch response simulations using PCA. For this, a dictionary of  $d = 113781$  atoms sampling the  $T1=[100:10:4000]$  (ms) and  $T2=[20:2:600]$  (ms) grid was simulated using the Extended Phase Graph formalism [46]. The subspace-compressed dictionary was directly used in DM and FGM, whereas for learning-based inference it was only used for training. Clean fingerprints were used for training MRFResnet decoder  $\mathcal{G}$  i.e. Bloch response generative network. Noisy fingerprints (i.i.d. noise  $\sim \mathcal{N}(0, 0.01)$ ) were used to train the MRFResnet encoder  $\mathcal{R}$ . After noise corruption (i.e. data augmentation by factor 50) we performed dictionary search to find correct (closest match) training labels and not those that originally generated the fingerprints in order to learn a projection mapping rather than a (possible overfitted) denoiser. Trainings used Adam optimiser with MSE loss for 20 epochs, 0.01 initial learning rate with decay factors 0.8/0.95 and mini-match sizes 500/20 for  $\mathcal{R}$  and  $\mathcal{G}$ , respectively. The same datasets were used for training KM's encoder and decoder models using LBFGS optimiser.

### C. Deep vs. shallow models' prediction results

To compare the prediction performances of the MRFResnet and KM models, 500K out-of-sample noisy fingerprints were randomly generated and fed to the encoder models to estimate T1/T2 parameters. Predicted T1/T2s were then fed to the decoder models for generating the corresponding noise-free Bloch responses. The ground-truth (GT) T1/T2s from DM were used to measure encoders' performances based on Mean Absolute (Percentage) Errors  $MAE = \mathbb{E}[|\hat{T}1 - T1^{GT}|]$  and  $MAPE = \mathbb{E}[\frac{|\hat{T}1 - T1^{GT}|}{T1^{GT}}]$  (similarly for T2). Corresponding clean fingerprints were used as GT to measure generative model (decoder) predictions based on Normalised-RMSE =  $\mathbb{E} \frac{\|\mathcal{G}(\hat{\Theta}) - \mathcal{B}(\Theta^{GT})\|}{\|\mathcal{B}(\Theta^{GT})\|}$ . Table I summarises our results.

	Total # params.	T1 (ms) MAE	T1 (%) MAPE	T2 (ms) MAE	T2 (%) MAPE	$\mathcal{B}$ (%) NRMSE
MRFResnet	5.2e3	7.2	0.9	1.9	1.0	0.8
KM fitting	18.0e4	28.3	3.7	21.2	11.6	13.3

TABLE I: Prediction performances of MRFResnet and KM.

<sup>6</sup>Used hyperparameters: FGM used 100 groups, KM used optimised kernel scales by MATLAB's `fitrkernel` function and 1000/500 random features [40] per output index for encoder/decoder models, respectively. VS used 880 shared views, LRTV used  $\forall i, \lambda_i = \lambda = 0.2/0.04$  for the 2D/3D scanned data.

1) *Discussion:* MRFResnet outperforms KM and achieves reliable predictions for T1/T2 values and Bloch response generation, with  $\leq 1\%$  average difference with the DM baseline. KM reports poor T2 and Bloch response estimations for the number of random features used. Comparing the size of both models we can deduce the advantage of *depth* in the proposed learning approach to embed DM, as compared to its shallow alternative for the adopted acquisition sequence.

#### D. In-vitro phantom experiment

The 2D (spiral/radial) 3D (spiral) acquisition schemes were tested for measuring quantitative parameters in twelve tubes of the EUROSPIN TO5 phantom. Figure 4 displays the mean and standard deviation of the predicted T1/T2 values in each ROI (tube) using different reconstructions algorithms: ZF, LR, VS and the proposed LRTV, all fed to the MRFResnet for quantitative inference. The spin-echo and inversion recovery spin-echo experiments suggested in the phantoms manual were used as references for T1/T2 values. Computed parameter map images are also shown in the supplementary materials. Figure 5 displays the Bland-Altman plots of the percentage differences between T1/T2 values of the phantom ROIs in spiral and radial scans, estimated using the ZF and LRTV.

1) *Discussion:* From Figure 4 we observe that tested methods (except VS for 2D<sup>7</sup>) report comparable performances in estimating mean T1/T2 values. T1 values are comparable to the GT (although ZF, LR and VS slightly underestimate T1). The predicted T2 values, especially in high T2 regimes, are under-estimated (negative bias).<sup>8</sup> Overall, the proposed LRTV predicts least biased T1/T2s. Notably, LRTV has the *least variations* around the estimated values. For all experiments and averaged over all ROIs, LRTV's standard deviation is 1.5/2.5 times less than its closest competitor for predicting T1/T2, respectively. Further, from Figure 5 we observe LRTV *enables highly consistent predictions* across different sampling protocols i.e. per-pixel estimated T1/T2 values in all ROIs obtained from radial and spiral measurements are 2 to 3 times more consistent with each other than those computed via ZF. We do not observe similar consistency level in other tested algorithms as the readout-dependent undersampling artefacts in images were not fully removed by them (Figure S2).

#### E. In-vivo 2D/3D experiments

We applied the same acquisition sequences for imaging a healthy volunteer's brain. Figures 6 displays the parametric maps reconstructed from 2D spiral and radial readouts. We computed the T1, T2 and proton density (PD) maps using reconstruction algorithms ZF, VS, LR and LRTV, and the MRFResnet for quantitative inference. We also tested KM inference after applying LRTV. For the 3D (spiral) acquisitions

<sup>7</sup>We observe VS generally trades off image smoothness against overestimated T2s and underestimated T1s. This compromise is strongly unfavourable in 2D acquisitions. Larger k-space neighbourhood information was available/shared in 3D (than 2D) acquisitions, which made 3D VS competitive.

<sup>8</sup>We hypothesize this is due to physical effects e.g. flip angle calibration errors, diffusion or magnetization transfer that are currently un-modelled in the reconstruction schemes.

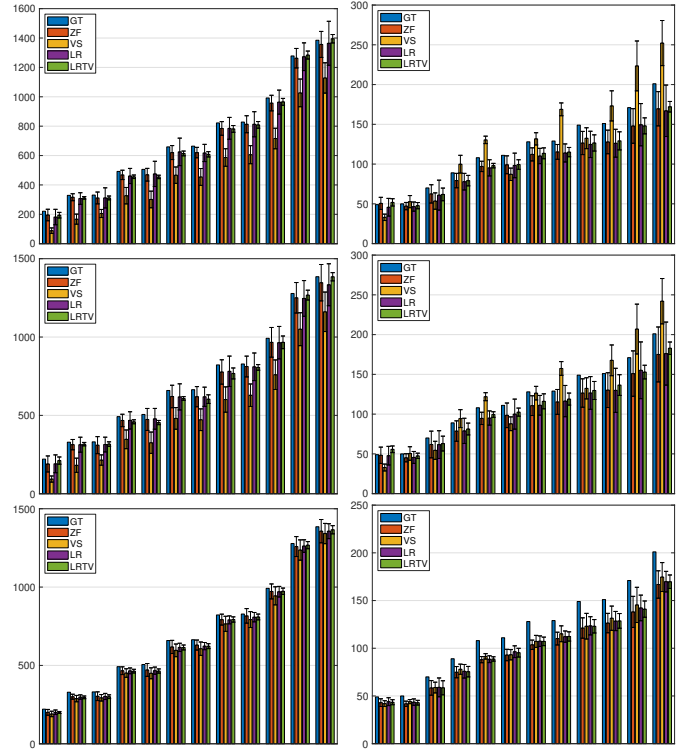


Fig. 4: The mean T1 (left column) and T2 (right column) values in milliseconds and their standard deviations (error bars) estimated via using four reconstruction methods compared to the reference values (GT) in 12 phantom ROIs. Results are compared for 2D spiral (top row), 2D radial (middle row) and 3D spiral acquisitions (bottom row).

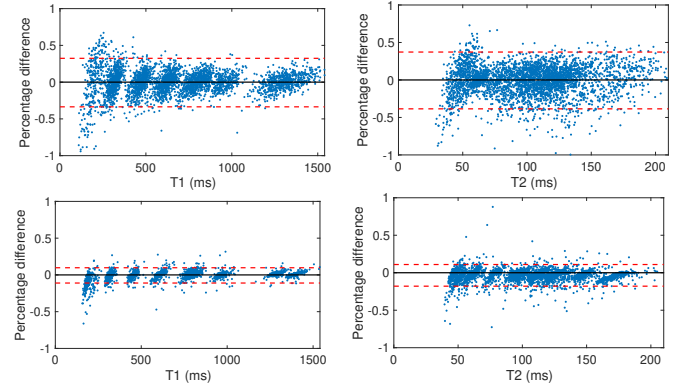


Fig. 5: Confidence intervals (CIs) for the percentage differences between predicted T1/T2 values of the phantom ROIs in spiral and radial scans, using ZF (top) and the LRTV (bottom) reconstructions. The 0.95%-CIs are -33.9% to 32.3% for T1 and -38.5% to 37.4% for T2 using ZF, whereas using LRTV CIs are tighter -10.2% to 7.8% for T1 and -17.0% to 10.4% for T2.

we compared LRTV and its closest competitor VS in Figure 7. Outcomes from other tested algorithm are displayed in the supplementary materials (Figure S3).

1) *Discussion:* The LRTV-MRFResnet outperforms all tested algorithms in reconstructing T1, T2 and PD maps in all acquisition schemes. Other methods were unable to successfully remove the under-sampling artefacts in TSMIs, and these errors propagated to the parameter inference phase and resulted in inaccurate maps. Temporal-only priors incorporated within LR are shown insufficient to regularise the inverse problem and LR sometimes (e.g. 2D spiral acquisitions) admits



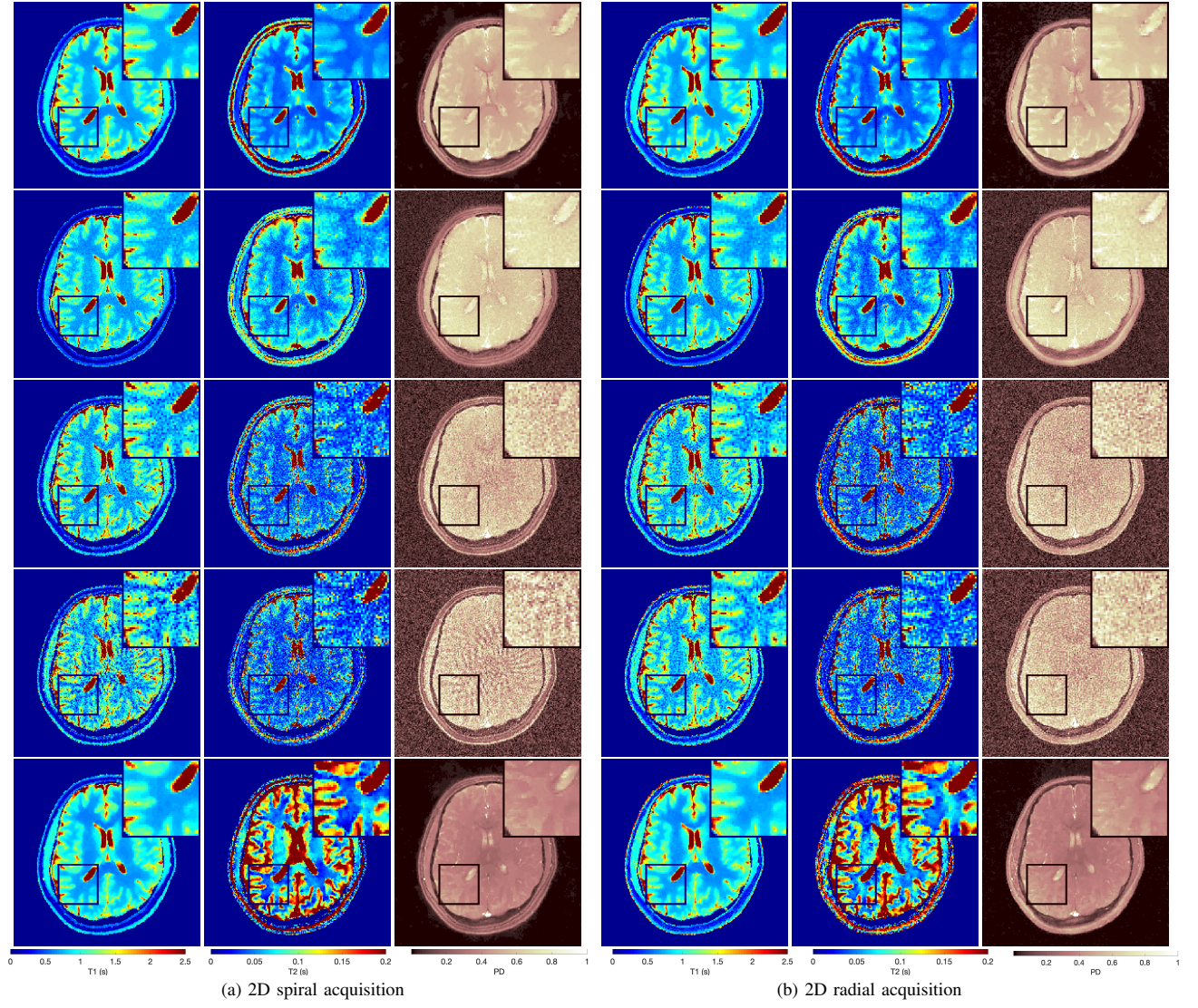


Fig. 6: Reconstructed T1, T2 and PD maps (left to right) from 2D (a) spiral and (b) radial scans using (from top to bottom) LRTV, VS, ZF and LR algorithms followed by MRFResnet inference and (the last row) LRTV with KM inference.

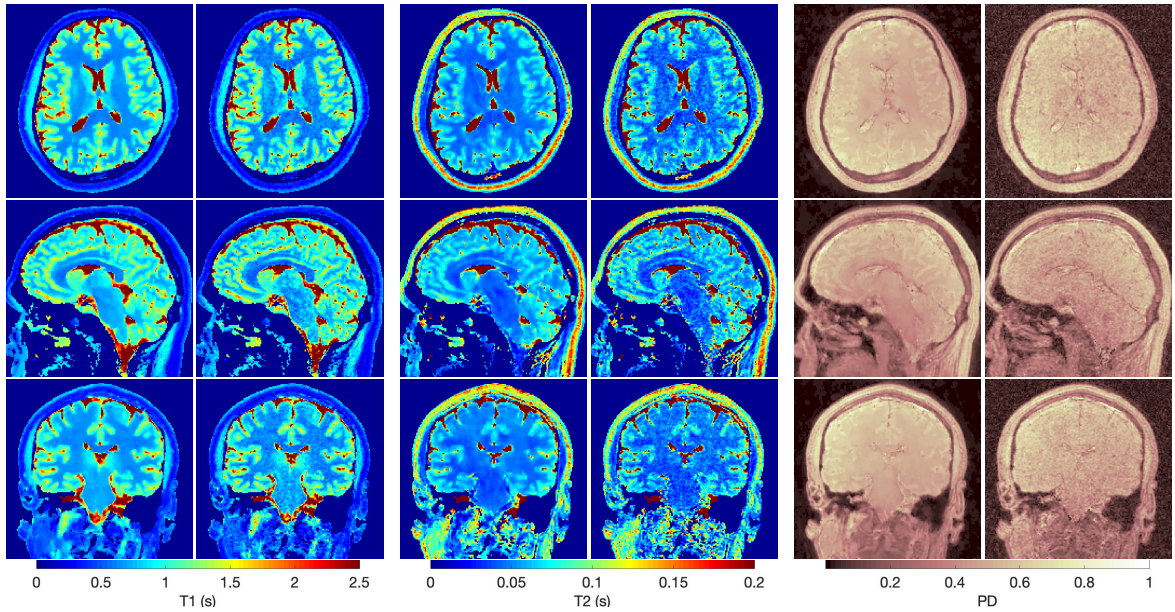


Fig. 7: Reconstructed T1 (first two columns) T2 (second two columns) and PD (third two columns) maps using a 3D scan with spiral readouts. The (zoomed) 3D maps are computed using LRTV (left sub-column) and VS (right sub-column) algorithms followed by MRFResnet for quantitative inference.



NRMSE (%)	T1	T2	PD
2D/3D phantom scans	0.08 / 0.13	0.12 / 0.13	0.78 / 1.43
2D/3D volunteer scans	3.25 / 1.28	7.15 / 2.68	4.34 / 6.04

TABLE II: NRMSE between the T1, T2 and PD maps obtained from MRFResnet and DM, after LRTV reconstruction.

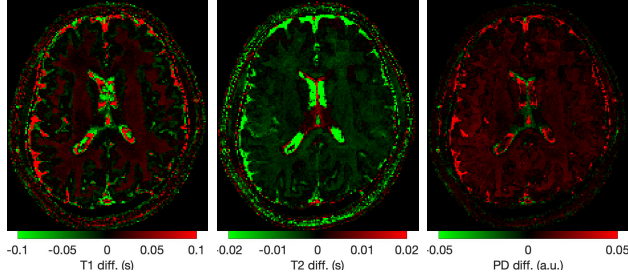


Fig. 8: Differences in the predicted T1 (left), T2 (middle) and PD (right) maps between MRFResnet and DM, after applying LRTV reconstruction.

solutions with even stronger artefacts than the model-free ZF baseline. This was previously observed for other non-Cartesian MRF readouts (e.g. [20, 19]), and highlights the need for adding appropriate spatial regularisation. The non model-based VS results in spatially smoother maps than ZF and LR, but is unable to fully clean the artefacts. Further and consistent with our *in-vitro* experiment, we observe that VS overestimates the PD and T2 values (e.g. in White and Grey matter regions) in tested 2D acquisitions (i.e. spatial regularisation trades off quantification accuracy). Finally, the learning-based KM and MRFResnet inference schemes applied after LRTV reconstruction, both output comparably accurate T1 maps. However the shallow KM model, despite having model size larger than MRFResnet, is unable to learn accurate T2 and PD quantification and results in poor estimated maps, consistent with our observations in section VI-C.

#### F. MRFResnet’s consistency with DM

Further to our validations in section VI-C, we compare parametric maps computed by DM and MRFResnet for the *in-vitro* and *in-vivo* experiments, where LRTV was applied for TSMI reconstruction. Results are summarised in Table II and for 2D spiral scans are illustrated in Figure 8. We observe very small differences in parametric maps (Table II) and particularly for the regions corresponding to white and grey matters predictions are highly consistent with each other (Figure 8).

#### G. Runtimes

Computations were conducted on an Intel Xeon E5-2667v4 processor (16 CPU cores), 32 GB RAM and a NVIDIA 2080Ti GPU. Where parallel computing was feasible, we adopted GPU implementation for speedup i.e. in forward/adjoint NUFFT operations [47], the TV shrinkage operator [48], VS, MRFResnet, DM and FGM. Table III includes computation times of the tested methods for the 2D/3D *in-vivo* experiments. LRTV benefits from momentum-acceleration and takes 7-11 iterations to converge, that is much faster than DM-based iterative methods (for comparisons see runtimes in [20]). We observed that the LR method without spatial regularisation makes very slow progress towards its (inaccurate) solution

and does not converge within our limit of 30 iterations. This indicates that exploiting additional (spatial) solution structure, despite introducing TV shrinkage computations, has an overall runtime advantage (see e.g.[49, 50]) by avoiding extra costly forward/adjoint iterations. The LRTV runs 2-3 times slower than its non-iterative competitor VS for achieving better predictions. DM-based inference methods are order(s) of magnitudes slower than MRFResnet, and therefore the great prediction consistency in both approaches suggests adopting neural inference in favour of runtime.

	reconstruction times (s)			prediction times (s)		
	ZF	VS	LRTV	DM	FGM	MRFResnet
2D	2.0	12.0	29.1	8.5	2.5	< 0.5
3D	148	913	2186	1901	789	54

TABLE III: Tested runtimes for quantitative brain image computing.

## VII. CONCLUSIONS

We proposed a two-stage DM-free approach for multi-parametric QMRI image computing based on compressed sensing reconstruction and deep learning. The reconstruction is convex and incorporates efficient spatiotemporal regularisations within an accelerated iterative shrinkage algorithm to minimise undersampling artefacts in the computed TSMI. We proposed MRFResnet, a compact auto-encoder network with deep residual blocks, in order to embed Bloch manifold projections through multi-scale piecewise affine approximations, and to replace the non-scalable DM baseline for quantitative inference. We demonstrated the effectiveness of the proposed scheme through validations on a novel 2D/3D multi-parametric quantitative acquisition sequence. Future extensions could address motion-artefacts and multi-compartment voxel quantification [51, 52] that are currently un-modelled in our pipeline. Further accelerations could be studied through stochastic gradients [53] and/or learned proximity operations [54] where the proposed scheme could complementarily be adopted for creating accurate labelled parametric maps for training.

## REFERENCES

- [1] P. Tofts, *Quantitative MRI of the brain: measuring changes caused by disease*. John Wiley & Sons, 2005.
- [2] D. Ma, V. Gulani, N. Seiberlich, K. Liu, J. Sunshine, J. Durek, and M. Griswold, “Magnetic resonance fingerprinting,” *Nature*, vol. 495, no. 7440, pp. 187–192, 2013.
- [3] N. Jiang Y, D. Ma, N. Seiberlich, V. Gulani, and M. Griswold, “MR fingerprinting using fast imaging with steady state precession (fisp) with spiral readout,” *Magnetic resonance in medicine*, vol. 74, no. 6, pp. 1621–1631, 2015.
- [4] B. Rieger, F. Zimmer, J. Zapp, S. Weingärtner, and L. R. Schad, “Magnetic resonance fingerprinting using echo-planar imaging: Joint quantification of T1 and T2\* relaxation times,” *Magnetic resonance in medicine*, vol. 78, no. 5, pp. 1724–1733, 2017.
- [5] K. L. Wright, Y. Jiang, D. Ma, D. C. Noll, M. A. Griswold, V. Gulani, and L. Hernandez-Garcia, “Estimation of perfusion properties with mr fingerprinting arterial spin labeling,” *Magnetic resonance imaging*, vol. 50, pp. 68–77, 2018.
- [6] Y. Jiang, J. Hamilton, W. Lo, K. Wright *et al.*, “Simultaneous T1, T2 and diffusion quantification using multiple contrast prepared magnetic resonance fingerprinting,” in *Proc. Intl. Soc. Mag. Res. Med.*, 2017.
- [7] M. Lustig, D. Donoho, and J. M. Pauly, “Sparse mri: The application of compressed sensing for rapid mr imaging,” *Magnetic Resonance in Medicine*, vol. 58, no. 6, pp. 1182–1195, 2007.

- [8] M. Davies, G. Puy, P. Vandergheynst, and Y. Wiaux, "A compressed sensing framework for magnetic resonance fingerprinting," *SIAM Journal on Imaging Sciences*, vol. 7, no. 4, pp. 2623–2656, 2014.
- [9] J. Assländer, M. A. Cloos, F. Knoll, D. K. Sodickson, J. Hennig, and R. Lattanzi, "Low rank alternating direction method of multipliers reconstruction for mr fingerprinting," *Magnetic resonance in medicine*, vol. 79, no. 1, pp. 83–96, 2018.
- [10] O. Cohen, B. Zhu, and M. S. Rosen, "MR fingerprinting deep reconstruction network (DRONE)," *Magnetic resonance in medicine*, vol. 80, no. 3, pp. 885–894, 2018.
- [11] P. Virtue, X. Y. Stella, and M. Lustig, "Better than real: Complex-valued neural nets for mri fingerprinting," in *Image Processing (ICIP), 2017 IEEE International Conference on*. IEEE, 2017, pp. 3953–3957.
- [12] M. Golbabaee, D. Chen, P. A. Gómez, M. I. Menzel, and M. E. Davies, "Geometry of deep learning for magnetic resonance fingerprinting," in *ICASSP 2019-2019 IEEE International Conference on Acoustics, Speech and Signal Processing (ICASSP)*, 2019, pp. 7825–7829.
- [13] E. Hoppe, G. Kördörfer, T. Würfl, J. Wetzl, F. Lugauer, O. Scheidegger, and A. Maier, "Deep learning for magnetic resonance fingerprinting: A new approach for predicting quantitative parameter values from time series," *Studies in health technology and informatics*, vol. 243, p. 202, 2017.
- [14] F. Balsiger, A. S. Konar, S. Chikop, V. Chandran, O. Scheidegger, S. Geethanath, and M. Reyes, "Magnetic resonance fingerprinting reconstruction via spatiotemporal convolutional neural networks," in *International Workshop on Machine Learning for Medical Image Reconstruction*. Springer, 2018, pp. 39–46.
- [15] Z. Fang, Y. Chen, M. Liu, L. Xiang, Q. Zhang, Q. Wang, W. Lin, and D. Shen, "Deep learning for fast and spatially-constrained tissue quantification from highly-accelerated data in magnetic resonance fingerprinting," *IEEE transactions on medical imaging*, 2019.
- [16] L. I. Rudin, S. Osher, and E. Fatemi, "Nonlinear total variation based noise removal algorithms," *Physica D: nonlinear phenomena*, vol. 60, no. 1–4, pp. 259–268, 1992.
- [17] D. F. McGivney, E. Pierre, D. Ma, Y. Jiang, H. Saybasili, V. Gulani, and M. A. Griswold, "SVD compression for magnetic resonance fingerprinting in the time domain," *IEEE transactions on medical imaging*, vol. 33, no. 12, pp. 2311–2322, 2014.
- [18] S. F. Cauley, K. Setsompop, D. Ma, Y. Jiang, H. Ye, E. Adalsteinsson, M. A. Griswold, and L. L. Wald, "Fast group matching for mr fingerprinting reconstruction," *Magnetic resonance in medicine*, vol. 74, no. 2, pp. 523–528, 2015.
- [19] C. C. Cline, X. Chen, B. Mailhe, Q. Wang, J. Pfeuffer, M. Nittka, M. A. Griswold, P. Speier, and M. S. Nadar, "Air-mrf: Accelerated iterative reconstruction for magnetic resonance fingerprinting," *Magnetic resonance imaging*, vol. 41, pp. 29–40, 2017.
- [20] M. Golbabaee, Z. Chen, Y. Wiaux, and M. Davies, "Coverblip: accelerated and scalable iterative matched-filtering for magnetic resonance fingerprint reconstruction," *Inverse Problems*, vol. 36, p. 015003, 2019.
- [21] S. Arberet, X. Chen, B. Mailhe, M. Nadar, and P. Speier, "Low rank and spatial regularization model for magnetic resonance fingerprinting," 2019, uS Patent 2019/0041480.
- [22] B. Zhao, K. Setsompop, E. Adalsteinsson, B. Gagoski, H. Ye, D. Ma, Y. Jiang, P. Ellen Grant, M. A. Griswold, and L. L. Wald, "Improved magnetic resonance fingerprinting reconstruction with low-rank and subspace modeling," *Magnetic resonance in medicine*, vol. 79, no. 2, pp. 933–942, 2018.
- [23] G. Mazor, L. Weizman, A. Tal, and Y. C. Eldar, "Low-rank magnetic resonance fingerprinting," *Medical physics*, vol. 45, no. 9, pp. 4066–4084, 2018.
- [24] I. Oksuz, G. Cruz, J. Clough, A. Bustin, N. Fuin, R. M. Botnar, C. Prieto, A. P. King, and J. A. Schnabel, "Magnetic resonance fingerprinting using recurrent neural networks," in *IEEE Intl. Symposium on Biomedical Imaging (ISBI)*, 2019, pp. 1537–1540.
- [25] G. Nataraj, J. Nielsen, C. Scott, and J. Fessler, "Dictionary-free mri perk: Parameter estimation via regression with kernels," *IEEE transactions on medical imaging*, vol. 37, no. 9, pp. 2103–2114, 2018.
- [26] E. Jaynes, "Matrix treatment of nuclear induction," *Physical Review*, vol. 98, no. 4, p. 1099, 1955.
- [27] A. Beck and M. Teboulle, "A fast iterative shrinkage-thresholding algorithm for linear inverse problems," *SIAM journal on imaging sciences*, vol. 2, no. 1, pp. 183–202, 2009.
- [28] Y. E. Nesterov, "A method for solving the convex programming problem with convergence rate  $O(1/k^2)$ ," in *Dokl. akad. nauk Sssr*, vol. 269, 1983, pp. 543–547.
- [29] A. Chambolle and T. Pock, "A first-order primal-dual algorithm for convex problems with applications to imaging," *Journal of Mathematical Imaging and Vision*, vol. 40, no. 1, pp. 120–145, 2011.
- [30] A. J. V. Benjamin, P. A. Gómez, M. Golbabaee, Z. B. Mahbub, T. Sprenger, M. I. Menzel, M. Davies, and I. Marshall, "Multi-shot echo planar imaging for accelerated cartesian mr fingerprinting: an alternative to conventional spiral mr fingerprinting," *Magnetic resonance imaging*, vol. 61, pp. 20–32, 2019.
- [31] M. Golbabaee and P. Vandergheynst, "Hyperspectral image compressed sensing via low-rank and joint-sparse matrix recovery," in *Acoustics, Speech and Signal Processing (ICASSP), 2012 IEEE International Conference on*. IEEE, 2012, pp. 2741–2744.
- [32] —, "Joint trace/tv norm minimization: A new efficient approach for spectral compressive imaging," in *Image Processing (ICIP), 2012 19th IEEE International Conference on*. IEEE, 2012, pp. 933–936.
- [33] P. Vincent, H. Larochelle, I. Lajoie, Y. Bengio, and P.-A. Manzagol, "Stacked denoising autoencoders: Learning useful representations in a deep network with a local denoising criterion," *Journal of machine learning research*, vol. 11, no. Dec, pp. 3371–3408, 2010.
- [34] M. Golbabaee, C. Pirkel, M. Menze, G. Bounincontri, and P. Gomez, "Deep MR fingerprinting with total-variation and low-rank subspace priors," in *Proceedings of Intl. Soc. Mag. Res. Med. (ISMRM)*, 2019.
- [35] M. Golbabaee, Z. Chen, Y. Wiaux, and M. Davies, "Cover tree compressed sensing for fast MR fingerprint recovery," in *IEEE Intl. Workshop on Machine Learning for Signal Processing*, 2017.
- [36] R. Balestrieri and richard baraniuk, "A spline theory of deep learning," in *Proceedings of the Intl. Conference on Machine Learning*, vol. 80, 2018, pp. 374–383.
- [37] G. F. Montufar, R. Pascanu, K. Cho, and Y. Bengio, "On the number of linear regions of deep neural networks," in *Advances in neural information processing systems*, 2014, pp. 2924–2932.
- [38] G. Cybenko, "Approximation by superpositions of a sigmoidal function," *Mathematics of control, signals and systems*, vol. 2, pp. 303–314, 1989.
- [39] O. Delalleau and Y. Bengio, "Shallow vs. deep sum-product networks," in *Advances in Neural Information Processing Systems*, 2011, pp. 666–674.
- [40] A. G. Wilson, Z. Hu, R. Salakhutdinov, and E. P. Xing, "Deep kernel learning," in *Artificial Intelligence and Statistics*, 2016, pp. 370–378.
- [41] K. Simonyan and A. Zisserman, "Very deep convolutional networks for large-scale image recognition," *arXiv preprint arXiv:1409.1556*, 2014.
- [42] R. Lerski and J. De Certaines, "Ii. performance assessment and quality control in mri by eurosip test objects and protocols," *Magnetic resonance imaging*, vol. 11, no. 6, pp. 817–833, 1993.
- [43] P. Gómez, M. Cencini, M. Golbabaee, R. Schulte, G. Fallo, L. Peretti, M. Tosetti, B. Menze, and G. Buonincontri, "Rapid three-dimensional multiparametric MRI with quantitative transient-state imaging," *arXiv preprint arXiv:2001.07173*, 2018.
- [44] G. Buonincontri and S. J. Sawiak, "Mr fingerprinting with simultaneous b1 estimation," *Magnetic resonance in medicine*, vol. 76, no. 4, pp. 1127–1135, 2016.
- [45] D. O. Walsh, A. F. Gmitro, and M. W. Marcellin, "Adaptive reconstruction of phased array mr imagery," *Magnetic Resonance in Medicine: An Official Journal of the International Society for Magnetic Resonance in Medicine*, vol. 43, no. 5, pp. 682–690, 2000.
- [46] M. Weigel, "Extended phase graphs: Dephasing, RF pulses, and echoes-pure and simple," *Journal of Magnetic Resonance Imaging*, vol. 41, no. 2, pp. 266–295, 2015.
- [47] <https://www.opensourceimaging.org/project/gpunuff/>.
- [48] <https://epfl-lts2.github.io/unlocbox-html/>.
- [49] V. Chandrasekaran and M. I. Jordan, "Computational and statistical tradeoffs via convex relaxation," *Proceedings of the National Academy of Sciences*, vol. 110, no. 13, pp. E1181–E1190, 2013.
- [50] J. Tang, M. Golbabaee, and M. Davies, "Gradient projection iterative sketch for large scale constrained least-squares," *Proceedings of the Intl. Conference on Machine Learning*, vol. 70, pp. 3377–3386, 2017.
- [51] G. Cruz, O. Jaubert, T. Schneider, R. M. Botnar, and C. Prieto, "Rigid motion-corrected magnetic resonance fingerprinting," *Magnetic resonance in medicine*, vol. 81, no. 2, pp. 947–961, 2019.
- [52] R. Duarte, A. Repetti, P. A. Gómez, M. Davies, and Y. Wiaux, "Greedy approximate projection for magnetic resonance fingerprinting with partial volumes," *arXiv preprint arXiv:1807.06912*, 2018.
- [53] J. Tang, K. Egiazarian, M. Golbabaee, and M. Davies, "The practicality of stochastic optimization in imaging inverse problems," *arXiv preprint arXiv:1910.10100*, 2019.
- [54] J. Tang, M. Golbabaee, F. Bach *et al.*, "Rest-katya: exploiting the solution's structure via scheduled restart schemes," in *Advances in Neural Information Processing Systems*, 2018, pp. 429–440.
- [55] <http://brainweb.bic.mni.mcgill.ca/brainweb/>.



## Supplementary Materials

### SI. IN-SILICO PHANTOM EXPERIMENT RESULTS

We further simulated the above-mentioned 2D spiral and radial acquisitions for measuring parametric maps in a slice of the *In-silico* Brainweb phantom [55]. A challenging single-coil acquisition with eight times less measurements were considered i.e.  $S(\tilde{X}) = \tilde{X}$  identity sensitivity map. Table I compares the reconstruction performances for the T1, T2, PD maps and the computed TSMIs using ZF, LR, VS and LRTV algorithms followed by the MRFResnet or KM for quantitative inference. Reconstructed maps are also shown in Figure S1.

	T1 MAPE	T2 MAPE	PD NRMSE	TMSI PSNR
ZF-DM	5.2 / 13.8	12.6 / 47.6	29.9 / 50.1	11.4 / 8.6
ZF-MRFResnet	5.5 / 15.6	12.1 / 51.4	49.50/ 60.7	—
VS-MRFResnet	8.6 / 11.3	46.0 / 48.4	33.2 / 37.8	14.0 / 13.1
LR-MRFResnet	7.7 / 11.6	12.7 / 20.7	25.8 / 30.6	13.6 / 12.6
LRTV-DM	3.2 / 3.9	9.6 / 11.0	12.2 / 18.4	14.8 / 14.6
LRTV-KM	3.4 / 4.3	33.0 / 36.2	23.2 / 31.8	—
<b>LRTV-MRFResnet</b>	<b>3.2 / 4.0</b>	<b>9.7 / 11.1</b>	<b>12.3 / 18.8</b>	<b>—</b>

TABLE I: The T1, T2 and PD maps’ MAPE and NRMSE errors (%), and the TSMI reconstruction PSNRs (dB) for the *in-silico* experiment. Results are sorted for the spiral / radial acquisitions and validated against the ground truth.

Results are consistent with those obtained in previous experiments. KM outputs inaccurate T2/PD predictions. Due to the extremely low k-space data for view sharing, VS also fails to recover T2 informations. Temporal priors used by LR are insufficient to reject under-sampling artefacts. On the other hand, the spatiotemporally regularised LRTV significantly improves TSMI reconstructions (e.g. 3 to 6 dB enhancement compared to the ZF baseline) through successfully removing strong aliasing artefacts (see Figure S1). This enables accurate parameter inference in the next stage using DM or the DM-free alternative MRFResnet. As can be seen in Table I, MRResnet and the DM baseline score competitive quantitative inference results regardless of the reconstruction algorithm.

### SII. *in-vitro* PHANTOM RECONSTRUCTED MAPS

In Figure S2 we display the computed T1, T2 and PD maps for our *in-vitro* phantom experiments in section VI-D. Tested reconstruction methods are ZF, LR, VS and the proposed LRTV, all fed to the MRFResnet for quantitative inference. Methods ZF and LR result in noisy predictions. It can be observed that for the 2D acquisitions (spiral/radial) VS strongly compromises between outputting smoother images and overestimated T2 values (bias). This issue is also present in *in-vivo* and *in-silico* experiments, where less k-space neighbourhood information are available to share (compared to the 3D acquisitions) and make the VS noncompetitive, and further the overall quantifications inconsistent across 2D/3D acquisitions. The proposed LRTV overcomes this issue through a model-based compressed sensing reconstruction.

### SIII. RECONSTRUCTED MAPS FOR THE 3D *in-vivo* SCANS

To supplement our comparisons in section VI-E (Figure 7) regarding the 3D quantitative brain imaging scans, we display the parametric maps (Figure S3) computed by the ZF and LR algorithms, both fed to the MRFResnet for quantitative inference. As can be seen, predictions are suffering from undersampling artefacts and are not competitive to those computed by the proposed LRTV algorithm (Figure 7).

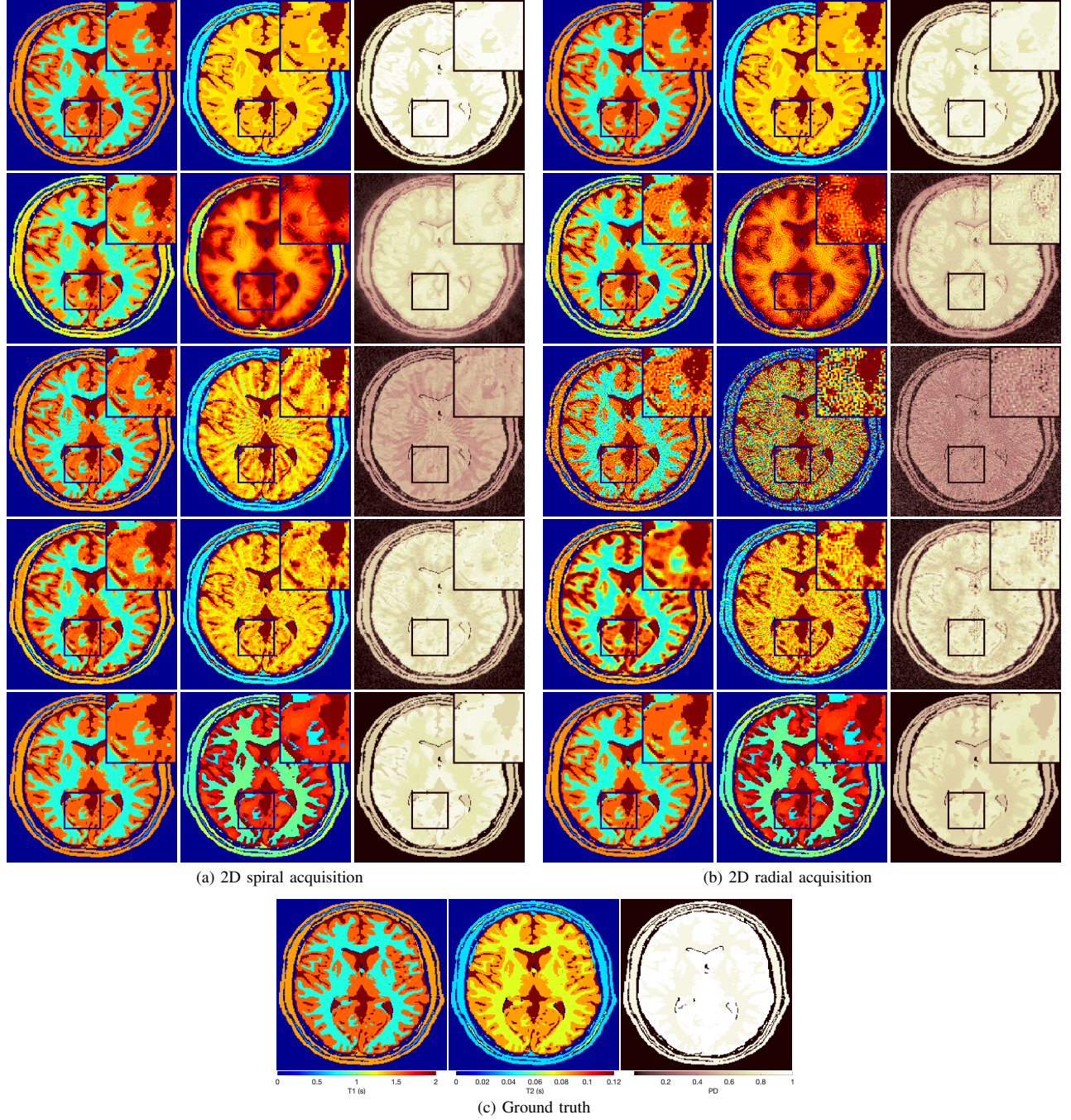


Fig. S1: Reconstructed T1, T2 and PD maps (left to right) from 2D (a) spiral and (b) radial simulated scans using (from top to bottom) LRTV, VS, ZF and LR algorithms followed by MRFResnet inference and (the last row) LRTV with KM inference. Figure (c) displays the ground truth maps used for simulations.

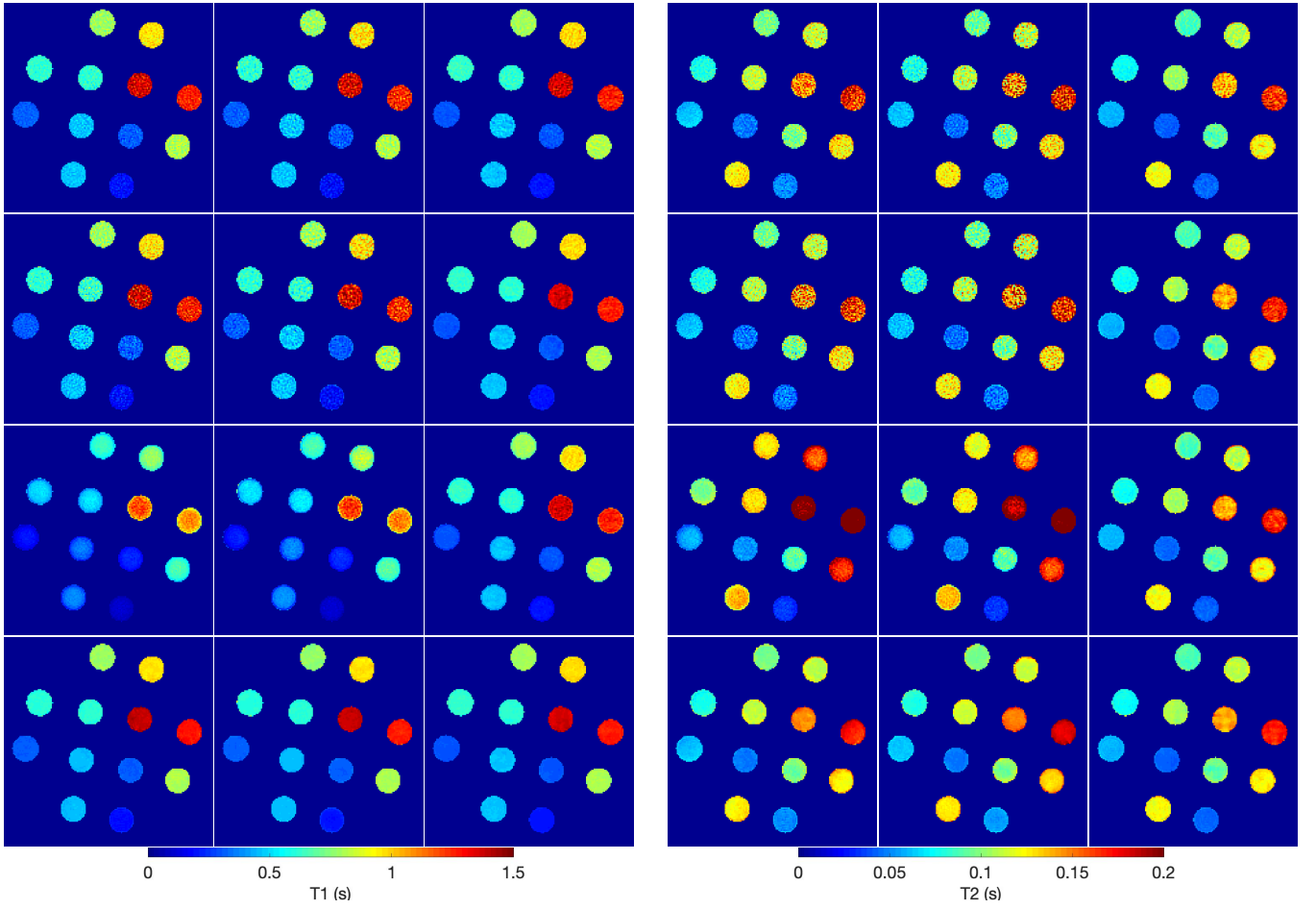


Fig. S2: Reconstructed T1 (3 left columns) and T2 (3 right columns) maps of EUROSPIN TO5 phantom, imaged using the 2D spiral (1st sub-column), 2D radial (2nd sub-column) and 3D spiral (3rd sub-column) k-space acquisitions. Tested reconstruction methods (from top to the bottom row) are ZF, LR, VS and LRTV, all fed to MRFResnet for inference.

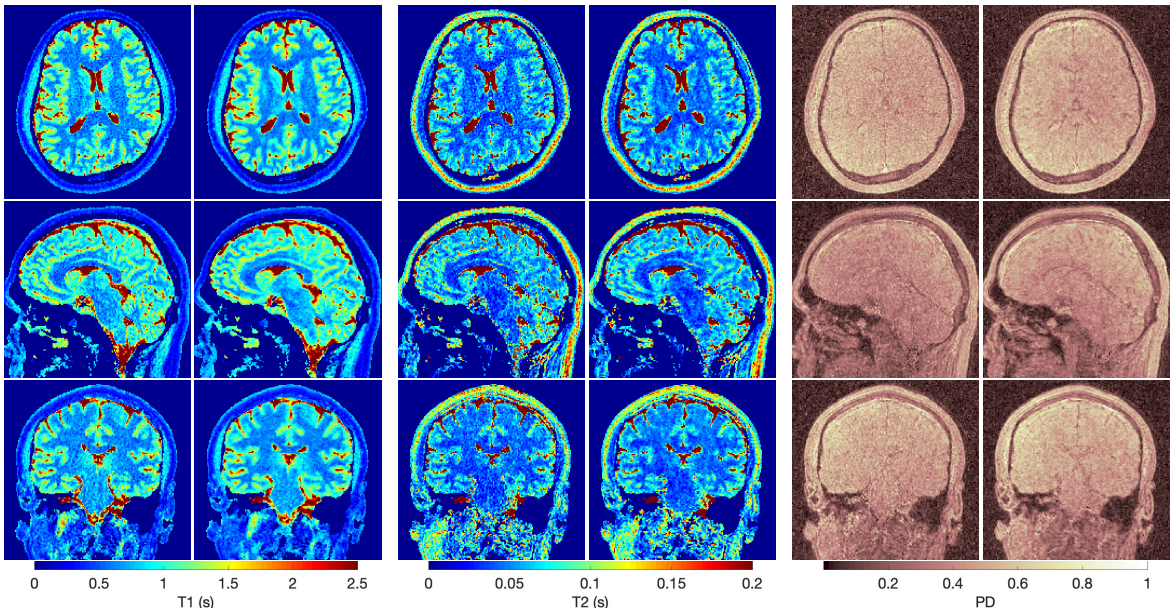


Fig. S3: Reconstructed T1 (first two columns) T2 (second two columns) and PD (third two columns) maps using a 3D scan with spiral readouts. The (zoomed) 3D maps are computed using ZF (left sub-column) and LR (right sub-column) algorithms followed by MRFResnet for quantitative inference.